

Bayesian Optimization for Function-Valued Responses under Min–Max Criteria

Pouya Ahadi

POUYA.AHADI@GATECH.EDU

*School of Industrial and Systems Engineering
Georgia Institute of Technology
Atlanta, GA 30332, USA*

Reza Marzban

MMARZBAN3@GATECH.EDU

*School of Electrical and Computer Engineering
Georgia Institute of Technology
Atlanta, GA 30332, USA*

Ali Adibi

ALI.ADIBI@ECE.GATECH.EDU

*School of Electrical and Computer Engineering
Georgia Institute of Technology
Atlanta, GA 30332, USA*

Kamran Paynabar*

KAMRAN.PAYNABAR@ISYE.GATECH.EDU

*School of Industrial and Systems Engineering
Georgia Institute of Technology
Atlanta, GA 30332, USA*

Abstract

Bayesian optimization is widely used for optimizing expensive black box functions, but most existing approaches focus on scalar responses. In many scientific and engineering settings the response is functional, varying smoothly over an index such as time or wavelength, which makes classical formulations inadequate. Existing methods often minimize integrated error, which captures average performance but neglects worst case deviations. To address this limitation we propose *min-max Functional Bayesian Optimization* (MM-FBO), a framework that directly minimizes the maximum error across the functional domain. Functional responses are represented using functional principal component analysis, and Gaussian process surrogates are constructed for the principal component scores. Building on this representation, MM-FBO introduces an integrated uncertainty acquisition function that balances exploitation of worst case expected error with exploration across the functional domain. We provide two theoretical guarantees: a discretization bound for the worst case objective, and a consistency result showing that as the surrogate becomes accurate and uncertainty vanishes, the acquisition converges to the true min-max objective. We validate the method through experiments on synthetic benchmarks and physics inspired case studies involving electromagnetic scattering by metaphotonic devices and vapor phase infiltration. Results show that MM-FBO consistently outperforms existing baselines and highlights the importance of explicitly modeling functional uncertainty in Bayesian optimization.

Keywords: Bayesian optimization, Gaussian processes, functional data analysis, robust optimization, min-max optimization

*. Corresponding author

1 Introduction

Bayesian optimization (BO) has become a mainstream strategy for optimizing expensive black box functions, owing to its high data efficiency and principled balance between exploration and exploitation (Wang et al., 2023; Shahriari et al., 2016). The framework has achieved remarkable success across diverse scientific and engineering domains, including aeronautical design, drug discovery, materials science, and automated machine learning (Liang et al., 2021; Candelieri, 2021). At its core, BO relies on probabilistic surrogate models and acquisition functions: Kotthoff et al. (2021) emphasizes that Gaussian processes are typically employed to capture uncertainty about the objective, while acquisition functions such as Expected Improvement guide sequential evaluations (Candelieri, 2021; Jones et al., 1998). This combination enables BO to identify promising solutions with far fewer evaluations than traditional search methods, making it especially suitable for applications where each experiment or simulation is costly.

Functional responses arise in many modern scientific and engineering problems where the output is not a single scalar but a curve defined over a continuous domain, such as time, wavelength, or angular response. In nanophotonics, for example, a device’s behavior might be fundamentally characterized by its spectral or angular response to an incident optical wavefront, which varies continuously across wavelength or incident angle and encodes rich underlying physics (Yu and Capasso, 2014; Kildishev et al., 2013; Chen et al., 2020). Because these responses must satisfy design objectives over an entire range rather than at a single operating point, inverse-design problems in photonics naturally take the form of functional optimization. Recent hybrid inverse-design frameworks have begun addressing this challenge by learning low-dimensional input-side representations (Marzban et al., 2025b) of the device geometry and then applying global or hybrid optimization methods to search this compressed design space for an optimal design (Chen et al., 2022; Marzban et al., 2025a,c; Kudyshev et al., 2020; Radford et al., 2025). These approaches are particularly effective in broadband and multifunctional settings where one seeks a single device that performs well across a continuous range of wavelengths. A common objective in these problems is to optimize a worst-case metric—such as maximizing the minimum diffraction or transmission efficiency across a target spectral band—which leads naturally to the min-max formulation considered here (Choi et al., 2024; Chen et al., 2022). Similar robust or worst-case formulations have also been central in earlier topology-optimized broadband photonic designs (Molesky et al., 2018; Pestourie et al., 2018). Beyond nanophotonics, function-valued outputs arise broadly in materials science, chemical reaction modeling, and complex engineering processes. In these applications, the full functional profile often carries crucial domain-specific information that cannot be captured by a single scalar summary (Conti and O’Hagan, 2010; Ren et al., 2021).

Existing approaches to functional data modeling and optimization often reduce function valued responses to scalar objectives by minimizing integrated error, typically in the form of mean squared error. While effective for capturing average performance, such scalarization can obscure variability across the functional domain and lead to solutions that are not robust to functional uncertainty. In BO of functional outputs for inverse problems, for example, directly modeling the function over its domain provides clearer guidance than collapsing

to a single scalar target (Huang et al., 2021). This perspective motivates methods that explicitly account for structure and uncertainty across the entire function.

A central focus of this work is the functional min-max formulation. Given a function $f(\theta, \lambda)$ defined over design variables $\theta \in \Theta$ and functional index $\lambda \in \Lambda$, the goal is to find

$$\theta^* \in \arg \min_{\theta \in \Theta} \max_{\lambda \in \Lambda} e(\theta, \lambda), \quad \text{where } e(\theta, \lambda) = (f(\theta, \lambda) - f^*(\lambda))^2,$$

and $f^*(\lambda)$ is the desired response as a function of lambda. This formulation contrasts with classical integrated error criteria, which emphasize average performance but may fail to capture the true worst-case behavior of functional responses. Recent studies in BO have begun to address such min-max structures. For example, Weichert and Kister (2021) introduced information based strategies to efficiently locate robust optima under min-max objectives, while Paulson et al. (2022) developed adversarially robust BO for controller auto tuning where the goal is to minimize the maximum loss under uncertainty. More recently, entropy-based approaches (Weichert et al., 2024) and scalable algorithms for arbitrary uncertain inputs (Yang et al., 2023) have further demonstrated the importance of directly modeling min-max criteria in Bayesian optimization. These works underscore the distinction between minimizing average error and directly targeting the worst case functional response.

Our work lies at the intersection of functional data analysis and BO. Functional data analysis provides a foundation for representing high-dimensional outputs as smooth curves, with functional principal component analysis (FPCA) and related tools serving to extract low dimensional representations of functional variability (Morris, 2015). These representations allow functional responses to be embedded into regression and prediction tasks by operating on principal component scores rather than full discretized functions. BO, on the other hand, has become the method of choice for optimizing expensive black box functions by combining Gaussian process surrogates with acquisition functions such as Expected Improvement (Jones et al., 1998; Shahriari et al., 2016). Notable examples include emulation of complex computer models with multi output or dynamic responses (Conti and O’Hagan, 2010) and BO of functional outputs in inverse problems (Huang et al., 2021). More recently, hybrid frameworks in nanophotonics have combined generative models (which learn an input-side representation) with BO to efficiently search for high-performance, multi-functional devices (Marzban et al., 2025a; Keawmuang et al., 2025). Our methodology formalizes the specific min-max objective function and provides the specialized acquisition strategy that is often implicit in these applied inverse-design challenges.

The contributions of this work are threefold. First, we propose Min–Max Functional Bayesian Optimization (MM-FBO), a new formulation of functional BO that directly targets the minimization of the maximum error across the functional domain, distinguishing it from prior approaches that rely on integrated error criteria. Second, we develop a methodology that combines FPCA with Gaussian process surrogates to represent and model functional responses efficiently, enabling the construction of an acquisition function that balances worst case exploitation with integrated exploration. Third, we provide two theoretical guarantees: a discretization error bound for the worst case objective and a consistency result showing that, as the surrogate becomes accurate and uncertainty vanishes, the acquisition converges to the true min-max objective. We then validate MM-FBO through extensive experiments on synthetic benchmarks and physics inspired case studies, demonstrating its value for BO when outputs are inherently functional rather than scalar.

We ground MM-FBO in two physics inspired studies that have function valued responses. First, in electromagnetics we design periodic metasurfaces that shape a scattering spectrum over a dense grid of wavelengths. Each candidate design is parameterized by a small set of geometric coefficients that define a supercell and the performance is the maximum squared deviation from a target spectrum across the wavelength range. This setting reflects common practice in metasurface design where spectra encode rich physical behavior and where dimensionality reduction and manifold ideas are natural tools (Yu and Capasso, 2014; Kildishev et al., 2013; Chen et al., 2020; Kiarashinejad et al., 2020; Zandehshahvar et al., 2022). Second, in materials processing we study vapor phase infiltration for polymer to inorganic hybrids, a process whose outcome is naturally represented as a function of time or dose. We connect this study to BO of functional outputs in inverse problems (Huang et al., 2021) and to core references that formalize the chemistry and process mechanisms of vapor phase infiltration and sequential infiltration synthesis (Leng and Losego, 2017; Waldman et al., 2019; Cara et al., 2021; Ren et al., 2021).

2 Problem Formulation

Many optimization tasks in science and engineering are characterized not by scalar outcomes but by functional responses. For example, in photonic design one may wish to match a desired scattering spectrum across the visible wavelength range; in electrochemistry the performance of a battery is observed as a capacity profile over time or cycles; and in energy harvesting radiative cooling materials are evaluated by their emissivity curves across a band of wavelengths. Unlike scalar-valued objectives, these responses are continuous functions of an auxiliary index, and the optimization task must account for discrepancies over the entire functional domain rather than at a single point. It is not sufficient for a design to perform well on average if it fails in even a small region of the domain. These examples motivate the need for optimization criteria that go beyond average error minimization.

Formally, let $\Theta \subset \mathbb{R}^d$ denote the compact design space and let Λ denote the compact functional domain. For each $\theta \in \Theta$ and $\lambda \in \Lambda$ the system returns a response

$$f : \Theta \times \Lambda \rightarrow \mathbb{R}, \quad (\theta, \lambda) \mapsto f(\theta, \lambda).$$

Given a target function $f^* : \Lambda \rightarrow \mathbb{R}$, we define the pointwise-squared error

$$e(\theta, \lambda) = (f(\theta, \lambda) - f^*(\lambda))^2, \quad \theta \in \Theta, \lambda \in \Lambda.$$

Two standard scalarizations are the integrated error and the worst-case error. The integrated error averages discrepancies across the domain,

$$\mathcal{I}(\theta) = \int_{\Lambda} e(\theta, \lambda) w(\lambda) d\lambda,$$

where w is an application specific weight function. This criterion rewards good average performance but can tolerate large local deviations. By contrast, the worst case error focuses on the maximum deviation,

$$g(\theta) = \sup_{\lambda \in \Lambda} e(\theta, \lambda) = \sup_{\lambda \in \Lambda} (f(\theta, \lambda) - f^*(\lambda))^2,$$

which requires uniform fidelity across the functional domain and penalizes any region with substantial departure from the target. We assume $f(\theta, \cdot)$ is continuous and square integrable on Λ , that observational noise ε has zero mean and bounded variance, and that Θ and Λ are compact. These assumptions ensure well-posedness of the optimization and enable functional analytic tools.

To summarize,

$$\theta^* \in \arg \min_{\theta \in \Theta} g(\theta), \quad \text{where} \quad g(\theta) = \sup_{\lambda \in \Lambda} (f(\theta, \lambda) - f^*(\lambda))^2.$$

This min-max formulation captures the requirement of uniform fidelity across the functional domain and differs fundamentally from minimizing integrated error, which prioritizes average performance. The remainder of the paper develops min-max Functional Bayesian Optimization, a BO methodology tailored to this formulation.

In applications with a discrete observation grid $\Lambda_T = \{\lambda_1, \dots, \lambda_T\}$ we write

$$g_T(\theta) = \max_{1 \leq m \leq T} e(\theta, \lambda_m).$$

To quantify how well g_T approximates g , define the fill distance

$$h_T = \sup_{\lambda \in \Lambda} \min_{1 \leq m \leq T} |\lambda - \lambda_m|.$$

We use a modulus of continuity, a nondecreasing function $\omega : [0, \infty) \rightarrow [0, \infty)$ with $\omega(0) = 0$ such that

$$|e(\theta, \lambda) - e(\theta, \lambda')| \leq \omega(|\lambda - \lambda'|) \quad \text{for all } \theta \in \Theta, \lambda, \lambda' \in \Lambda.$$

When $e(\theta, \lambda)$ is Lipschitz in λ uniformly in θ with constant L , this specializes to $\omega(r) = Lr$.

Proposition 1 *Assume $e(\theta, \lambda)$ admits a modulus of continuity ω uniformly in θ as above. Then for every $\theta \in \Theta$,*

$$0 \leq g(\theta) - g_T(\theta) \leq \omega(h_T).$$

If, in addition, $e(\theta, \lambda)$ is L Lipschitz in λ uniformly in θ , then

$$g(\theta) - g_T(\theta) \leq L h_T.$$

In the one-dimensional case with $\Lambda = [a, b] \subset \mathbb{R}$ and an equally spaced grid of T points with spacing $\Delta = (b - a)/(T - 1)$, the fill distance is $h_T = \Delta/2$, hence

$$g(\theta) - g_T(\theta) \leq \omega(\Delta/2), \quad \text{and, if Lipschitz,} \quad g(\theta) - g_T(\theta) \leq \frac{L}{2} \Delta.$$

A complete proof of Proposition 1 is provided in Appendix A. Proposition 1 shows that g_T uniformly approaches g as the grid densifies, which justifies using a discrete grid when only sampled functional responses are available.

3 Methodology

Having established the problem formulation, we now turn to the development of a BO framework that can effectively handle function-valued responses under a min–max objective. The key challenge is that directly modeling the error surface $e(\theta, \lambda)$ over both θ and λ is computationally intractable due to its infinite-dimensional nature. To address this, we employ functional data analysis tools to obtain a parsimonious representation of responses, which can then be modeled using Gaussian processes within the BO loop. In particular, we rely on FPCA to project functional responses into a low-dimensional latent space while retaining their dominant modes of variation. For consistency, we denote design variables by $\theta \in \Theta$ and the functional index by $\lambda \in \Lambda$.

3.1 FPCA Representation

Consider the set of functional responses $\{f(\theta_j, \cdot)\}_{j=1}^N$ obtained from N design evaluations. Each function $f(\theta_j, \lambda)$ is assumed to lie in $L^2(\Lambda, \nu)$, the Hilbert space of square-integrable functions on Λ with inner product

$$\langle g_1, g_2 \rangle = \int_{\Lambda} g_1(\lambda) g_2(\lambda) d\nu(\lambda).$$

FPCA seeks an orthonormal basis $\{\phi_i(\lambda)\}_{i=1}^{\infty}$, called functional principal components (FPCs), that diagonalize the covariance operator of the sample. Each response can then be expressed in its truncated Karhunen–Loève expansion as

$$f(\theta, \lambda) \approx \bar{f}(\lambda) + \sum_{i=1}^M c_i(\theta) \phi_i(\lambda),$$

where $\bar{f}(\lambda)$ is the sample mean function and $\{\phi_i(\lambda)\}_{i=1}^M$ are the retained functional principal components. For a given design θ , the coefficient

$$c_i(\theta) = \int_{\Lambda} (f(\theta, \lambda) - \bar{f}(\lambda)) \phi_i(\lambda) d\lambda$$

is the i th principal component (PC) score, summarizing how the response at design θ projects onto mode ϕ_i . These scores provide a finite-dimensional representation of the functional response: once $\{c_i(\theta)\}$ are known, the function $f(\theta, \cdot)$ can be accurately reconstructed. Consequently, our surrogate modeling effort focuses on learning the mapping $\theta \mapsto c_i(\theta)$, which transfers the problem from functional outputs to a set of scalar regression tasks. Truncation to M terms is justified by the decay of eigenvalues in the Karhunen–Loève expansion, so that the leading M FPCs capture the vast majority of functional variability.

The benefit of FPCA is twofold. First, it reduces infinite-dimensional functional responses into a finite vector of PC scores $(c_1(\theta), \dots, c_M(\theta))$, enabling standard multivariate modeling. Second, the orthogonality of the basis ensures that variability along distinct components is uncorrelated in the training sample, simplifying surrogate modeling. In this work we fit independent Gaussian process (GP) surrogates to each score:

$$c_i(\theta) \sim \text{GP}(\mu_i(\theta), k_i(\theta, \theta')), \quad i = 1, \dots, M,$$

where μ_i and k_i denote the mean and kernel functions, respectively. Independence of scores is assumed for computational tractability; in practice, we assess this by examining sample correlations among estimated scores. Empirically, our experiments show that optimization performance is robust to mild violations of independence.

3.2 Error Process and Distribution

We model the pointwise deviation from the target as

$$h(\theta, \lambda) = f(\theta, \lambda) - f^*(\lambda),$$

so that $e(\theta, \lambda) = h(\theta, \lambda)^2$. Under the FPCA representation,

$$h(\theta, \lambda) \approx \delta(\lambda) + \Phi(\lambda)^\top \mathbf{c}(\theta) + r(\lambda),$$

where $\delta(\lambda) = \bar{f}(\lambda) - f^*(\lambda)$, $\Phi(\lambda) = (\phi_1(\lambda), \dots, \phi_M(\lambda))^\top$, $\mathbf{c}(\theta) = (c_1(\theta), \dots, c_M(\theta))^\top$, and $r(\lambda)$ is the truncation error. With Gaussian score posteriors $\mathbf{c}(\theta) \sim \mathcal{N}(\boldsymbol{\mu}_c(\theta), \boldsymbol{\Sigma}_c(\theta))$ and an independent mean zero residual process r , the deviation $h(\theta, \lambda)$ is Gaussian with mean and variance

$$\mu_h(\theta, \lambda) = \delta(\lambda) + \Phi(\lambda)^\top \boldsymbol{\mu}_c(\theta), \quad \sigma_h^2(\theta, \lambda) = \Phi(\lambda)^\top \boldsymbol{\Sigma}_c(\theta) \Phi(\lambda) + \sigma_r^2(\lambda).$$

Its covariance kernel is

$$K_h(\theta; \lambda, \lambda') = \Phi(\lambda)^\top \boldsymbol{\Sigma}_c(\theta) \Phi(\lambda') + R(\lambda, \lambda'),$$

where R is the covariance of r .

For a fixed pair (θ, λ) , the deviation can be written as a Gaussian random variable

$$Z = h(\theta, \lambda) \sim \mathcal{N}(\mu_h(\theta, \lambda), \sigma_h^2(\theta, \lambda)).$$

We can then define the standardized variable

$$U = \frac{Z - \mu_h(\theta, \lambda)}{\sigma_h(\theta, \lambda)} \sim \mathcal{N}(0, 1),$$

which facilitates characterization of the distribution of the squared error $e(\theta, \lambda) = Z^2$.

Then

$$e(\theta, \lambda) = Z^2 = \sigma_h^2 \left(U + \frac{\mu_h}{\sigma_h} \right)^2 = \sigma_h^2 X, \quad \text{where } X \sim \chi_1^2(\lambda_{\text{nc}}), \quad \lambda_{\text{nc}} = \left(\frac{\mu_h}{\sigma_h} \right)^2.$$

Hence e/σ_h^2 is noncentral chi square with one degree of freedom and noncentrality λ_{nc} . A convenient closed form for the pdf of e follows from the change of variables $y = Z^2$ with two inverse branches $Z = \pm\sqrt{y}$:

$$f_e(y | \theta, \lambda) = \frac{1}{\sigma_h \sqrt{2\pi} y} \exp\left(-\frac{y + \mu_h^2}{2\sigma_h^2}\right) \cosh\left(\frac{\mu_h \sqrt{y}}{\sigma_h^2}\right), \quad y > 0.$$

From the noncentral chi-square moments or directly from Gaussian moments,

$$\mathbb{E}[e(\theta, \lambda)] = \mu_h^2(\theta, \lambda) + \sigma_h^2(\theta, \lambda), \quad \text{Var}[e(\theta, \lambda)] = 2\sigma_h^4(\theta, \lambda) + 4\mu_h^2(\theta, \lambda)\sigma_h^2(\theta, \lambda).$$

For two indices λ, λ' , let $h = h(\theta, \lambda)$ and $h' = h(\theta, \lambda')$ be jointly Gaussian with means $\mu_h, \mu_{h'}$, variances $\sigma_h^2, \sigma_{h'}^2$, and covariance $K_h(\theta; \lambda, \lambda')$. Using Gaussian fourth moment identities,

$$\text{Cov}(e(\theta, \lambda), e(\theta, \lambda')) = 2K_h(\theta; \lambda, \lambda')^2 + 4\mu_h(\theta, \lambda)\mu_h(\theta, \lambda')K_h(\theta; \lambda, \lambda').$$

These expressions permit closed-form evaluation of pointwise error statistics and their dependence across the domain, with cost $\mathcal{O}(M^2)$ per evaluation of (μ_h, σ_h^2) , reduced to $\mathcal{O}(M)$ when independent score posteriors make $\Sigma_c(\theta)$ diagonal.

3.3 Acquisition Function with Integrated Uncertainty

Direct modeling of the distribution of the min–max objective

$$g(\theta) = \sup_{\lambda \in \Lambda} e(\theta, \lambda)$$

is analytically intractable, since it requires characterizing the supremum of a noncentral chi-square process. Moreover, simulation-based approximations such as extreme value sampling or posterior draws over dense grids are computationally expensive and unstable in high dimensions. To avoid these issues, we design an acquisition function that approximates the spirit of the min–max criterion while remaining tractable.

Our acquisition combines two complementary elements: the worst-case expected error and an integrated measure of predictive uncertainty. Formally,

$$\alpha(\theta) = \max_{\lambda \in \Lambda} \mu_e(\theta, \lambda) - \kappa \int_{\Lambda} \sigma_e(\theta, \lambda) d\nu(\lambda),$$

where $\mu_e(\theta, \lambda) = \mathbb{E}[e(\theta, \lambda)]$ and $\sigma_e^2(\theta, \lambda) = \text{Var}(e(\theta, \lambda))$.

The first term, $\max_{\lambda} \mu_e(\theta, \lambda)$, reflects the predicted worst-case error. By minimizing this quantity the search focuses on designs that reduce the maximum deviation from the target across the functional domain. The second term, $\int_{\Lambda} \sigma_e(\theta, \lambda) d\nu(\lambda)$, quantifies overall uncertainty. Its role is to encourage exploration in regions where the error process is poorly understood, ensuring that the optimization does not become trapped by spurious local minima of the mean predictor. The trade-off parameter $\kappa > 0$ balances exploitation of the worst-case prediction with exploration guided by integrated uncertainty.

In practice, the integral is replaced by a weighted sum

$$\int_{\Lambda} \sigma_e(\theta, \lambda) d\nu(\lambda) \approx \sum_{m=1}^T w_m \sigma_e(\theta, \lambda_m),$$

with w_m representing quadrature weights or uniform averaging depending on the application. This maintains computational efficiency while preserving a rigorous connection to the continuous formulation.

A static choice of κ may either over-emphasize exploration or prematurely focus on exploitation. We therefore adjust κ dynamically across iterations: it is inflated in early stages to ensure coverage of the design space, decreased as convergence stabilizes to accelerate refinement, and increased again if progress stagnates to escape local traps. This adaptation

requires only simple heuristics, yet significantly improves robustness in practice. This acquisition strategy sidesteps the intractability of directly modeling the supremum distribution of $g(\theta)$ while still capturing the essence of the min–max problem. By explicitly combining worst-case predictions with integrated uncertainty and adaptively balancing the two, our framework enables principled and efficient optimization of functional objectives.

In practice, optimization of the acquisition function $\alpha(\theta)$ is performed by combining global exploration with local refinement. Candidate starting points are generated by space-filling designs or random sampling across Θ , and from each start a local optimizer such as L-BFGS or quasi-Newton search is applied. Multiple restarts mitigate the risk of local traps, while diversity constraints prevent redundant evaluations near previously sampled points. In low-dimensional settings, grid-based initialization is especially effective, whereas in higher dimensions random restarts dominate. This strategy ensures reliable identification of promising designs without requiring exact global optimization of the acquisition. A complete description of our procedure is summarized in Algorithm 1, which highlights the key steps of MM-FBO. By Theorem 2, as modeling error decreases and uncertainty collapses, minimizing the acquisition targets the true worst case objective.

Asymptotic fidelity of the acquisition. As the surrogate improves, the acquisition should track the true worst-case objective. The result below formalizes this idea. It shows that when the mean predictor of the squared error is uniformly accurate and the integrated uncertainty vanishes while the exploration weight stays bounded, the acquisition surface converges uniformly to the true worst-case objective. Hence, any near minimizer of the acquisition converges to a true minimizer of the min-max target.

Theorem 2 (Consistency of the acquisition under vanishing uncertainty) *Let $\{\mu_{e,t}, \sigma_{e,t}\}_{t \geq 1}$ be the iteration indexed error moments and define*

$$\alpha_t(\theta) = \max_{\lambda \in \Lambda} \mu_{e,t}(\theta, \lambda) - \kappa_t \int_{\Lambda} \sigma_{e,t}(\theta, \lambda) d\nu(\lambda).$$

Assume:

- (i) *Uniform mean accuracy:* $\sup_{(\theta, \lambda) \in \Theta \times \Lambda} |\mu_{e,t}(\theta, \lambda) - e(\theta, \lambda)| \rightarrow 0.$
- (ii) *Vanishing integrated uncertainty:* $\sup_{\theta \in \Theta} \int_{\Lambda} \sigma_{e,t}(\theta, \lambda) d\nu(\lambda) \rightarrow 0.$
- (iii) *Bounded exploration weight:* $\sup_t \kappa_t < \infty.$
- (iv) *Existence of a minimizer:* Θ is compact and $g(\theta) = \sup_{\lambda \in \Lambda} e(\theta, \lambda)$ attains its minimum on $\Theta.$

Then $\sup_{\theta \in \Theta} |\alpha_t(\theta) - g(\theta)| \rightarrow 0.$ Consequently, any sequence $\{\theta_t\}$ with $\alpha_t(\theta_t) \leq \inf_{\theta} \alpha_t(\theta) + o(1)$ has all its limit points in the set of minimizers of $g.$

A complete proof of Theorem 2 is provided in Appendix B.

Algorithm 1 Min-Max Functional Bayesian Optimization (MM-FBO)

Require: Initial set size n_0 , total budget N , retained components M

- 1: **Initialize** $\{\theta_j\}_{j=1}^{n_0}$ by space filling; evaluate $f(\theta_j, \cdot)$
 - 2: **FPCA** on observed responses; retain M components
 - 3: **Fit GPs** to score maps $\theta \mapsto c_i(\theta)$ for $i = 1, \dots, M$
 - 4: **while** evaluations $< N$ **do**
 - 5: Compute $\mu_h(\theta, \lambda)$ and $\sigma_h^2(\theta, \lambda)$
 - 6: Obtain $\mu_e(\theta, \lambda)$ and $\sigma_e^2(\theta, \lambda)$
 - 7: Form $\alpha(\theta) = \max_{\lambda} \mu_e(\theta, \lambda) - \kappa \int_{\Lambda} \sigma_e(\theta, \lambda) d\nu(\lambda)$
 - 8: $\theta_{\text{next}} \leftarrow \arg \min_{\theta} \alpha(\theta)$ using multi start local search with restarts and diversity constraints
 - 9: Evaluate $f(\theta_{\text{next}}, \cdot)$; update FPCA if needed; refit GPs; adapt κ
 - 10: **end while**
 - 11: **return** $\theta^* = \arg \min_{\theta \in \{\text{evaluated}\}} \max_{\lambda} \mu_e(\theta, \lambda)$
-

4 Experiments

We now evaluate the proposed methodology through a combination of controlled benchmarks and physics-inspired case studies. The experimental study is designed to test both accuracy and robustness under different conditions, with particular emphasis on functional responses where reliability across the entire domain is critical. Each experiment follows the same overall protocol: functional responses are generated or collected over a domain Λ , an initial set of space-filling designs is evaluated, and sequential optimization proceeds under a fixed budget. The proposed acquisition with adaptive strategies is compared against established baselines to assess improvements in convergence speed, stability, and worst-case performance.

Our evaluation proceeds in two stages. First, we consider synthetic benchmark functions, where the true optimum g^* and the exact error process can be computed. These functions enable systematic exploration across dimensions and replication to quantify variability. Second, we turn to physics-inspired case studies drawn from real engineering problems, including photonic metasurface design to provide a desired scattering spectrum and polymer-inorganic hybrid formation via vapor phase infiltration. In both settings functional responses arise naturally and robustness to local deviations is essential. To contextualize performance we compare MM-FBO against a set of baselines: (i) Latin Hypercube Design (LHD), a static space-filling design (SFD) that provides a non-adaptive benchmark; (ii) standard Bayesian optimization, which fits a GP surrogate to the scalarized objective $g(\theta) = \max_{\lambda} e(\theta, \lambda)$ and selects new points via Expected Improvement. In practice we also employ simple variants of $\alpha(\theta)$ that adapt across phases of the search, beginning with broad exploration, transitioning to a balanced criterion, and ending with refinement that leverages local uncertainty.

Performance is quantified through both trajectory-based and summary metrics. The primary trajectory measure is the regret curve

$$r_k = g(\theta_k^{\text{best}}) - g^*, \quad \theta_k^{\text{best}} = \arg \min_{j \leq k} g(\theta_j),$$

which records how the best observed design improves over k iterations. Median regret with interquartile ranges is reported across replications to capture stability. To summarize overall efficiency we compute the area under the normalized regret curve (AUOC),

$$\text{AUOC} = \frac{1}{B} \sum_{k=1}^B \frac{r_k}{r_0},$$

where B is the evaluation budget and r_0 is the initial regret. Lower AUOC indicates faster and more consistent convergence. We also report the distribution of final regrets at budget B , and the time-to-threshold (TT) statistic

$$\text{TT}_\epsilon = \min\{k : r_k \leq \epsilon\},$$

which measures the iteration count required to reach accuracy ϵ . Together, these metrics provide a comprehensive view of convergence speed, robustness across replications, and worst-case accuracy.

4.1 Simulation Study

We evaluate the proposed method on a suite of time-dependent simulation oracles that generate function-valued responses over a dense grid of the index variable λ , interpreted as time. The problems span a range of dimensions and dynamic behaviors, providing a diverse testbed. For each oracle we define a reference response $f^*(\lambda)$ at a known target parameter θ^* and measure performance through the worst-case deviation objective

$$g(\theta) = \sup_{\lambda \in \Lambda} (f(\theta, \lambda) - f^*(\lambda))^2.$$

The first oracle is the **mass–spring–damper system**, a classical model in vibration analysis where damping and natural frequency determine stability and oscillatory behavior. The design vector is $\theta = (\zeta, \omega_n) \in \mathbb{R}^2$ and the index is time $\lambda = t$. The displacement $y(t; \zeta, \omega_n)$ under a unit step input satisfies

$$\ddot{y}(t) + 2\zeta\omega_n\dot{y}(t) + \omega_n^2y(t) = 1, \quad y(0) = 0, \dot{y}(0) = 0.$$

We define the functional response as

$$f(\theta, t) = y(t; \zeta, \omega_n),$$

so the objective measures the displacement curve’s deviation from a desired target response $f^*(t)$.

The second oracle is the **susceptible–infected–recovered (SIR) epidemic model**, a standard tool in epidemiology for characterizing disease spread. The design vector is $\theta = (\beta, \gamma, I_0) \in \mathbb{R}^3$, and the index is time $\lambda = t$. With initial conditions $S(0) = 1 - I_0$, $I(0) = I_0$ and $R(0) = 0$, the dynamics are

$$\frac{dS}{dt} = -\beta SI, \quad \frac{dI}{dt} = \beta SI - \gamma I, \quad \frac{dR}{dt} = \gamma I.$$

The functional response is defined as

$$f(\theta, t) = I(t; \beta, \gamma, I_0),$$

the infection trajectory whose shape is critical in public health modeling.

The third oracle is the **Lotka–Volterra predator–prey system**, a nonlinear model from ecology describing interactions between predator and prey populations. The design vector is $\theta = (\alpha, \beta, \delta, \gamma) \in \mathbb{R}^4$, and the index is time $\lambda = t$. With initial conditions $x(0) = y(0) = 1$, the dynamics are

$$\frac{dx}{dt} = \alpha x - \beta xy, \quad \frac{dy}{dt} = \delta xy - \gamma y.$$

The functional response is defined as

$$f(\theta, t) = x(t; \alpha, \beta, \delta, \gamma),$$

capturing prey population trajectories across time.

The fourth oracle is the **one-dimensional heat diffusion model**, a partial differential equation (PDE) that is fundamental in thermal engineering and materials science. The design vector is $\theta = (\kappa, L, T_L, T_R, q, \alpha, \beta) \in \mathbb{R}^7$, with $\lambda = t$ indexing time. On $x \in [0, L]$, the temperature satisfies

$$\frac{\partial u}{\partial t} = \kappa \frac{\partial^2 u}{\partial x^2} + q, \quad u(0, t) = T_L, \quad u(L, t) = T_R,$$

with initial condition $u(x, 0) = \alpha + \beta \sin(\pi x/L)$. The functional response is taken at mid depth,

$$f(\theta, t) = u(L/2, t; \kappa, L, T_L, T_R, q, \alpha, \beta),$$

yielding a one-dimensional time series that reflects transient thermal behavior.

Together these oracles test the method across diverse mathematical structures: linear ordinary differential equations (ODEs), nonlinear compartmental models, nonlinear predator–prey dynamics, and parabolic PDEs, with varying dimensionality and temporal complexity. We visualize typical responses from each oracle. Figure 1 shows multiple random trajectories for each system across the time domain, illustrating the variety of shapes and scales that motivate a worst-case objective.

All experiments share a common protocol. A budget of $m = 50$ sequential evaluations is allowed after an initial set of n_0 seeds obtained via Latin hypercube sampling. At each iteration we form a candidate set by combining a global Sobol pool with a local pool around the current best design. Candidates are first ranked by an exploitation score, after which the integrated uncertainty acquisition with adaptive κ selects the next evaluation, with occasional pure exploitation steps to accelerate progress. We compare against two standard baselines: a Gaussian process fit directly to the scalar objective $g(\theta)$ with expected improvement, and a progressive space-filling design that is not adaptive. Each configuration is run for $R = 50$ independent replications with shared seeds and candidate pools, enabling paired comparisons. Performance is assessed through four complementary metrics: regret trajectories, normalized regret trajectories, final regret distributions, and AUOC. To further

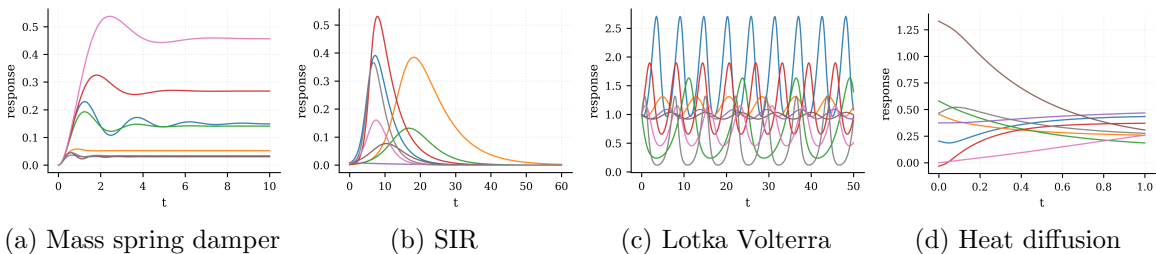


Figure 1: Representative trajectories drawn from each simulator. Each panel shows multiple random draws of the response over time to illustrate functional variability across the design space.

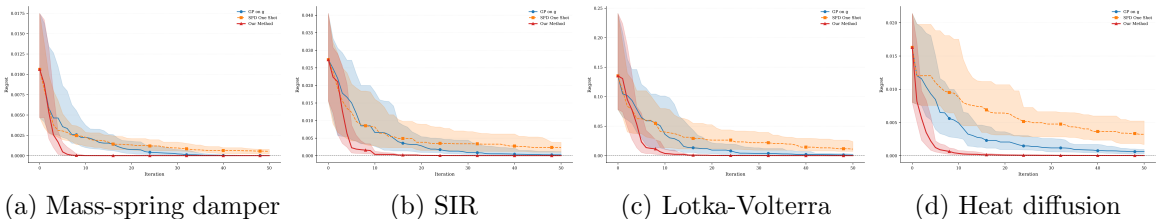


Figure 2: Regret versus iteration with median and interquartile bands.

quantify sample efficiency, we also report the time to threshold (TT) defined as the iteration at which regret first falls below ϵ .

The results are summarized in four panels. Figure 2 presents regret versus iteration across the four problems. Our method consistently converges faster and reaches lower regret values compared with both baselines. The improvement is most pronounced in the mass–spring–damper and heat–diffusion systems, where clear separation appears within the first few iterations and is maintained throughout. In the SIR and Lotka–Volterra systems the advantage is still evident, but emerges more gradually as the dynamics introduce oscillatory or nonlinear interactions that pose greater challenges for scalar approaches. Figure 3 reports the normalized regret trajectories, which emphasize stability across replications. Normalization makes clear that our method not only converges earlier but also exhibits substantially tighter interquartile bands, reflecting more reliable performance across independent runs. Figure 4 shows the distribution of final regret after the evaluation budget is exhausted. Across all four problems, our method achieves markedly smaller medians and interquartile spreads, confirming that the best-found solutions are consistently closer to the reference function. Complementing this perspective, Figure 5 summarizes the area under the normalized regret curve (AUOC), which integrates performance over the entire trajectory. Here again our method achieves the smallest values across problems, underscoring superior sample efficiency. Finally, Tables 1 and 2 report the time to threshold (TT) metric for $\epsilon = 0.10$ and $\epsilon = 0.05$, respectively. Each entry shows the fraction of successful runs together with the median iteration required to cross the threshold. The results demonstrate that our method reaches both thresholds in nearly all replications and does so in far fewer iterations than either baseline.

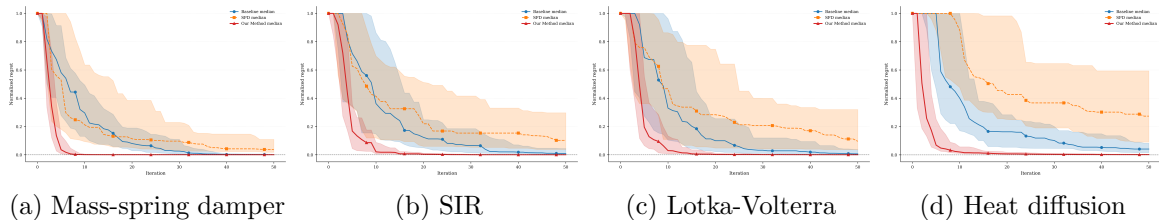


Figure 3: Normalized regret trajectories showing convergence speed and stability.

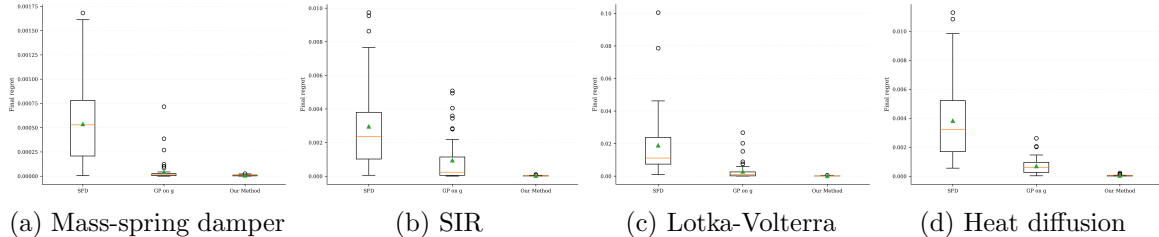


Figure 4: Box plots of final regret distributions across replications.

Across all metrics and problems, the proposed method is consistently superior. It converges faster in terms of regret trajectories, is more stable under normalization, achieves substantially smaller final regret, and exhibits lower AUOC values that confirm improved sample efficiency. The TT results further show that thresholds of both $\epsilon = 0.10$ and $\epsilon = 0.05$ are reached reliably and in far fewer iterations. Particularly in challenging problems such as heat diffusion and Lotka-Volterra, where functional responses display sharp features and oscillations, the benefits of balancing worst-case error with integrated uncertainty are most pronounced.

4.2 Case Studies

We next ground the methodology in physics-inspired case studies where the response is a function of wavelength λ or time t , and the design vector θ collects geometric or process parameters. In both settings, the objective remains to minimize the worst-case squared deviation from a prescribed target response. For the metasurface scattering problem, the target is the flat scattering spectrum $f^*(\lambda) \equiv 1$, reflecting the goal of broadband scattering with high efficiency as the high response. For the vapor phase infiltration process, the target $f^*(t)$ is a reference infiltration profile obtained from physical considerations, where fidelity to the entire curve rather than any single time point is critical. Throughout, we denote by $\Lambda = \{\lambda_1, \dots, \lambda_T\}$ or $\{t_1, \dots, t_T\}$ the discretized functional domain and by $\Theta \subset \mathbb{R}^p$ a bounded hyper-rectangle of admissible designs.

Case Study 1: Design of Metasurfaces for Wideband Scattering in Photonics.

This study considers photonic metasurfaces engineered to control an optical wavefront via subwavelength geometric patterning. The selected metasurface is a periodic structure with a supercell formed by 16×16 cylindrical rods with arbitrary radii (larger than a minimum value assigned by fabrication limitations) located in a regular grid, as shown in Figure 6 (a). This results in an excessive number (256) of design parameters for the radii of the rods.

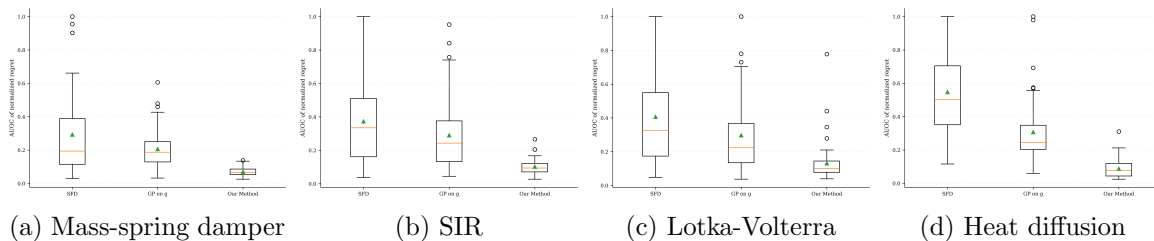


Figure 5: AUOC distributions summarizing full regret trajectories.

 Table 1: Time to threshold (TT) results for $\epsilon = 0.10$. Each entry shows fraction of successful runs and median iteration.

Problem	SFD	GP on g	MM-FBO
Mass spring damper	0.74 (15)	0.98 (18)	1.00 (5)
SIR	0.48 (14)	0.84 (20)	1.00 (7)
Lotka Volterra	0.52 (11)	0.86 (18)	0.98 (8)
Heat diffusion	0.32 (25)	0.80 (25)	1.00 (5)

To reduce this number, we use a Fourier like parameterization of the pillar radius profile over the in plane coordinates (x, y) of a unit cell with periods $(\text{period}_x, \text{period}_y)$. Writing $\omega_x = \frac{2\pi}{\text{period}_x}$ and $\omega_y = \frac{2\pi}{\text{period}_y}$, a representative truncated expansion is

$$R(x, y; \theta) = r_0 [A_0 + A_1 \sin(\omega_x x + \omega_y y) + A_2 \cos(\omega_x x + \omega_y y) + A_3 \sin(2(\omega_x x + \omega_y y)) + A_4 \cos(2(\omega_x x + \omega_y y)) + \dots],$$

where the amplitudes $\{A_\ell\}$ and base scale r_0 are components of θ . Together with additional layout parameters (for example unit cell period, aspect controls, and thickness) these coefficients define the super cell geometry from which the scattering spectrum $H(\lambda; \theta)$ is generated by a full wave electromagnetic solver (see Figure 6 (b) for a visualization). This parameterization is based on the recently demonstrated GiBS framework, which represents the entire device geometry using a compact set of coefficients from smooth parametric bases (for example Fourier or Chebyshev) (Marzban et al., 2025c). This input side representation drastically compresses the design space for full-wave optimization methods such as Bayesian optimization.

The goal of the inverse design is to find these geometrical parameters that define the shape of the metasurface with the best response. Each candidate design $\theta \in \Theta \subset \mathbb{R}^{14}$ specifies a set of geometric coefficients that modulate a periodic array of nano pillars as shown in Figure 6, producing a scattering spectrum $H(\lambda; \theta)$ over a dense grid of wavelengths. Our target response is a broadband highly efficient uniform scattering spectrum; accordingly, we define the loss at design θ as

$$g(\theta) = \max_{\lambda \in \Lambda} (H(\lambda; \theta) - 1)^2, \quad \text{with } f^*(\lambda) = 1.$$

We assembled a dataset of $N = 4000$ designs, each paired with a measured/simulated spectrum sampled at $T = 201$ wavelengths, i.e., $\{(\theta_i, \{H(\lambda_t; \theta_i)\}_{t=1}^T)\}_{i=1}^N$. The wavelength

Table 2: Time to threshold (TT) results for $\epsilon = 0.05$. Each entry shows fraction of successful runs and median iteration.

Problem	SFD	GP on g	MM-FBO
Mass spring damper	0.60 (23)	0.94 (25)	1.00 (5)
SIR	0.30 (19)	0.78 (25)	1.00 (10)
Lotka Volterra	0.34 (10)	0.82 (20)	0.98 (10)
Heat diffusion	0.12 (23)	0.62 (29)	0.96 (6)

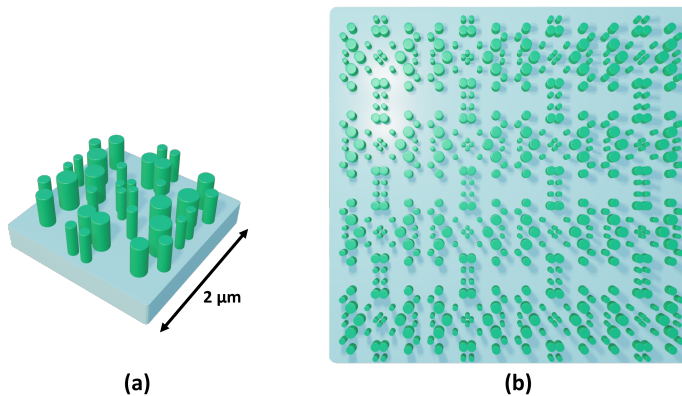


Figure 6: Schematic of a metasurface generated through a basis-driven geometric parameterization. The structure is designed to maximize the broadband scattering cross-section and is composed of 200 nm-thick dielectric nanopillars on a silicon oxide (SiO_2) substrate. (a) Isometric view of the nanopillars within a $2 \mu\text{m} \times 2 \mu\text{m}$ supercell. (b) Top view of the full metasurface, where the radius and lateral position of each nanopillar are modulated by a smooth basis function. This basis is defined by a compact set of geometric coefficients (θ), enabling a low-dimensional representation of an otherwise complex, large-area design.

grid Λ spans the band of interest with increasing resolution where resonant structure is anticipated. Bounds for each coordinate of θ define a box-constrained domain $\Theta = [\ell_1, u_1] \times \dots \times [\ell_{14}, u_{14}]$ used in all optimization runs. For each candidate design we computed the scattering spectrum on a dense wavelength grid across the band of interest Λ , with design variables sampled uniformly within the admissible bounds described above. All full-wave electromagnetic simulations were performed using three-dimensional finite-difference time-domain (3D FDTD) technique (implemented using the commercial software Lumerical) on periodic supercell geometries of Figure 6 (b).

Because the dataset is fixed, we emulate the oracle $H(\lambda; \theta)$ with a fast, differentiable surrogate trained once on all (θ, λ) pairs and then used for on-the-fly evaluations. Concretely, we fit a low-rank separable neural model

$$\widehat{H}(\lambda; \theta) = a(\theta)^\top b(\lambda),$$

in which $a : \Theta \rightarrow \mathbb{R}^r$ and $b : \Lambda \rightarrow \mathbb{R}^r$ are shallow networks and λ is encoded with Fourier features to capture oscillatory structure. Inputs θ are standardized, wavelengths are scaled

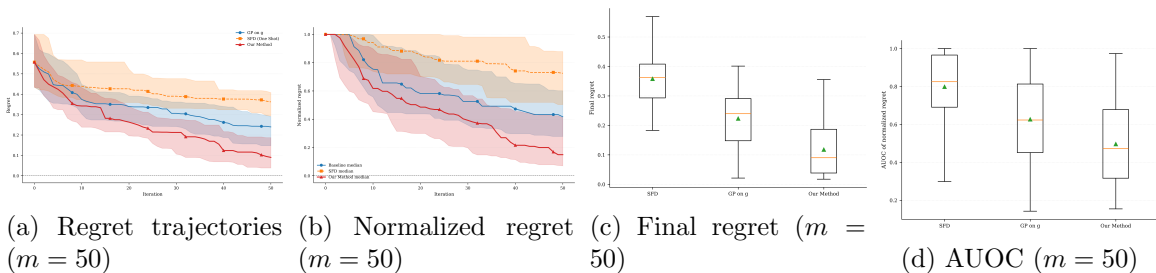


Figure 7: Electromagnetic scattering results with budget $m = 50$. Our method achieves smaller and more stable regret trajectories, lower AUOC, and significantly better time-to-threshold performance compared with both baselines.

Table 3: TT results for electromagnetic scattering with $m = 50$. Each entry shows fraction of successful runs and median iteration. “—” indicates that the threshold was not reached within the budget.

ε	SFD	GP on g	MM-FBO
0.10	0.00 (—)	0.08 (41)	0.42 (40)
0.05	0.00 (—)	0.02 (42)	0.14 (36)

to $[0, 1]$, and responses are standardized during training and mapped back to physical units at inference time.

The optimization results for the electromagnetic scattering case study are summarized in Figures 7 and 8, with corresponding TT metrics reported in Tables 3 and 4. We first consider the low-budget setting with $m = 50$ evaluations after seeding. Figure 7 (a) shows the regret trajectories across methods. Our approach rapidly drives regret toward zero, reaching very small values well within the budget, whereas the GP on g baseline converges more slowly and the space-filling design (SFD) stagnates at substantially higher levels. Normalized regret curves in Figure 7 (b) reinforce this observation: our method exhibits a sharp and stable descent with minimal interquartile spread, in contrast to the wider bands of the two baselines. Distributional summaries are shown in panels Figures 7 (c) and 7 (d): the boxplots indicate that our method achieves significantly smaller final regret and AUOC values, with both medians and interquartile ranges markedly below those of GP on g and SFD. Specifically, the median final regret is 0.0902 for our method compared with 0.2396 for GP on g and 0.3624 for SFD, while AUOC values are 0.4720, 0.6233, and 0.8253 respectively. The TT analysis in Table 3 shows that at $\varepsilon = 0.10$, our method succeeds in 42% of runs with a median crossing at iteration 40, while GP on g manages only 8% at iteration 41 and SFD fails entirely. Even under the stricter $\varepsilon = 0.05$, our method still crosses in 14% of runs, whereas the two baselines remain almost uniformly unsuccessful.

The high-budget setting with $m = 100$ evaluations paints an even clearer picture (Figure 8). Regret trajectories in Figure 8 (a) show that our method not only descends more steeply but also stabilizes at values close to zero, whereas GP on g continues to oscillate and the SFD regret trajectory remains high. Normalized regret in Figure 8 (b) confirms this stability and shows that our method maintains a consistently smaller band of variation

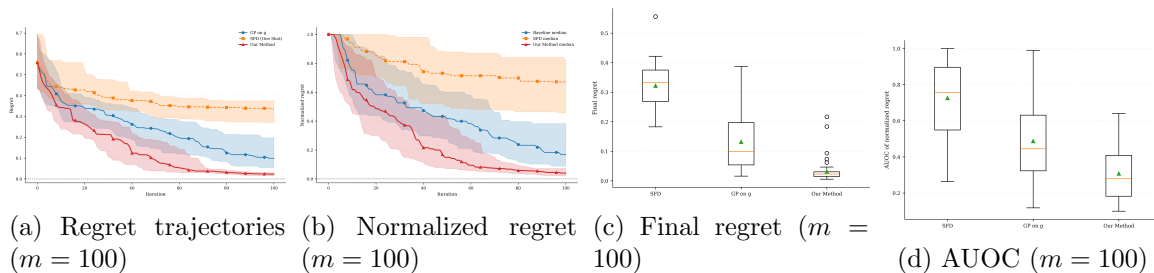


Figure 8: Electromagnetic scattering results with budget $m = 100$. Larger budget accentuates the advantage of our method, which consistently dominates both baselines across all metrics.

Table 4: TT results for electromagnetic scattering with $m = 100$. Each entry shows fraction of successful runs and median iteration. “–” indicates that the threshold was not reached within the budget.

ε	SFD	GP on g	MM-FBO
0.10	0.00 (–)	0.32 (80)	0.88 (55)
0.05	0.00 (–)	0.12 (68)	0.58 (72)

across replications. The boxplots in Figures 8 (c) and 8 (d) demonstrate that both final regret and AUOC values are dramatically reduced, with much tighter interquartile ranges than in the low-budget case. Quantitatively, the median final regret is only 0.0229 for our method, compared with 0.0990 for GP on g and 0.3331 for SFD, while AUOC values fall to 0.2793, 0.4451, and 0.7567, respectively. The TT results in Table 4 now show 88% of runs successfully crossing $\varepsilon = 0.10$ with a median of just 55 evaluations in our approach, compared with 32% at iteration 80 for GP on g and no success for SFD. Even under $\varepsilon = 0.05$, our method succeeds in 58% of runs, far above the 12% achieved by GP on g .

Taken together, these results show that the proposed acquisition function achieves consistent and substantial improvements over scalar-objective baselines. The improvements manifest not only in the final regret but also in the entire optimization trajectory, as measured by AUOC and TT. The gains are particularly pronounced under tighter budgets, underscoring the value of balancing exploration and exploitation across the functional domain.

Case Study 2: Vapor-Phase Infiltration in Polymer Films. Vapor-phase infiltration (VPI) is a hybrid materials processing technique in which organic polymers are exposed to vapor-phase metal–organic precursors that sorb, diffuse, and eventually react within the polymer matrix, producing durable organic–inorganic composites with enhanced mechanical, optical, and thermal properties (Huang et al., 2021; Ren et al., 2021). Unlike traditional atomic layer deposition (ALD), which coats surfaces conformally, VPI achieves subsurface infiltration by coupling precursor transport with polymer–precursor reactions. This process has been applied to membranes, sensors, hybrid optics, and structural reinforcements.

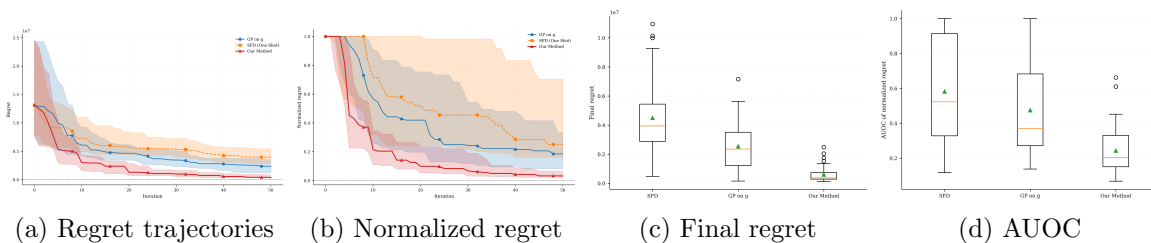


Figure 9: VPI results. Our method achieves markedly smaller final regret and AUOC, with faster TT compared to both SFD and GP on g .

From a modeling perspective, simple Fickian diffusion is inadequate to describe VPI since the infiltrating precursor both diffuses and reacts irreversibly with polymer functional groups. A reaction–diffusion framework captures these coupled effects (Ren et al., 2021). Let $C_{\text{free}}(x, t)$ denote the local concentration of free precursor, $C_{\text{polymer}}(x, t)$ the concentration of accessible reactive groups, and $C_{\text{product}}(x, t)$ the concentration of immobilized product. The governing equations are

$$\frac{\partial C_{\text{free}}}{\partial t} = D(C_{\text{product}}) \frac{\partial^2 C_{\text{free}}}{\partial x^2} - k C_{\text{free}} C_{\text{polymer}}, \quad (1)$$

$$\frac{\partial C_{\text{product}}}{\partial t} = k C_{\text{free}} C_{\text{polymer}}, \quad (2)$$

$$D(C_{\text{product}}) = D_0 \exp(-K' C_{\text{product}}), \quad (3)$$

$$\frac{\partial C_{\text{polymer}}}{\partial t} = -k C_{\text{free}} C_{\text{polymer}}, \quad (4)$$

with D_0 being the fresh diffusivity, k the second-order rate constant, and K' a hindering constant that encodes how immobilized product reduces free volume and transport. Nondimensionalization yields a set of key parameters: the Damköhler number $Da = k C_{\text{polymer}}^0 L^2 / D_0$, the ratio $C_s / C_{\text{polymer}}^0$ of surface concentration to initial reactive groups, and the hindering number $K' C_{\text{polymer}}^0$, which jointly dictate whether infiltration is diffusion-limited, reaction-limited, or hindered.

We adopt this VPI case study following Huang et al. (2021) as a benchmark for functional BO under reaction diffusion uncertainty. In this setting the functional index is time t with domain \mathcal{T} , and the objective is

$$g(\theta) = \max_{t \in \mathcal{T}} (H(t; \theta) - f^*(t))^2.$$

Here $H(t; \theta)$ denotes the predicted infiltration uptake over time for design θ , and $f^*(t)$ is the target infiltration profile. We set $f^*(t)$ to the trajectory generated at a designated reference design θ^* , which represents a physically meaningful configuration of the process and yields an attainable performance level.

The optimization outcomes are summarized in Figure 9. Regret trajectories (Figure 9 (a)) show that our method rapidly reduces error, while the baselines converge more slowly and with higher variability. Normalized regret (Figure 9 (b)) confirms stability: the spread of our method is narrower and consistently below alternatives. Final performance comparisons in Figures 9 (c) and 9 (d) highlight substantial improvements: median final regret

Table 5: Time to threshold (TT) results for VPI. Each entry shows fraction of successful runs and median iteration.

ε	SFD	GP on g	MM-FBO
0.10	0.10 (14)	0.35 (25)	0.85 (20)
0.05	0.03 (17)	0.17 (35)	0.72 (33)

drops to 3.74×10^5 for our method versus 2.35×10^6 (GP on g) and 3.94×10^6 (SFD), while AUOC values are reduced to 0.2042 compared with 0.3692 and 0.5227 respectively. These gains indicate that our method not only finds better solutions but does so more efficiently across the entire budget.

Time-to-threshold (TT) metrics in Table 5 further underscore this advantage. At $\varepsilon = 0.10$, our method succeeds in 85% of runs within a median of 20 iterations, compared to 35% at iteration 25 for GP on g and only 10% at iteration 14 for SFD. Under the stricter $\varepsilon = 0.05$, our method still achieves 72% success at iteration 33, well above the 17% for GP on g and the negligible 3% for SFD. Thus, our proposed approach consistently accelerates convergence toward high-quality infiltration designs.

Taken together, the VPI case study demonstrates that balancing exploration over functional responses yields dramatic performance gains. Unlike the baselines, which struggle under the coupled reaction–diffusion dynamics, our method leverages the full functional structure to achieve both lower regret and faster attainment of practically relevant error thresholds.

5 Discussion and Conclusion

This work introduced a framework for BO tailored to function-valued responses under a min–max criterion. By combining FPCA with Gaussian process surrogates, we derived an acquisition function that explicitly balances worst-case exploitation with integrated exploration. Our experiments across synthetic oracles, physics-inspired simulations, and case studies in metaphotonics and VPI demonstrate that our proposed method consistently achieves lower regret, faster convergence, and improved stability compared with established baselines.

From a theoretical perspective, the results highlight the importance of moving beyond integrated-error formulations toward explicit worst-case modeling. The min–max objective, though more challenging analytically, provides stronger guarantees of uniform fidelity across the functional domain. Our acquisition design leverages closed-form error statistics to achieve computational tractability while ensuring asymptotic convergence of the acquisition to the target objective. These contributions extend the BO theory into settings where functional responses and robustness requirements are central.

Practically, the methodology offers clear benefits for engineering and scientific applications. In metaphotonic design, it identifies geometries that maintain high scattering response across the entire wavelength range rather than only on average. This directly addresses the challenge of designing multifunctional and broadband nanophotonics devices, where hybrid design frameworks are already employing BO to solve worst-case objectives

(e.g., maximizing minimum efficiency) in compressed latent spaces. Our MM-FBO framework provides the formal, efficient acquisition strategy needed for exactly these types of problems, moving beyond standard Expected Improvement used on scalarized objectives. In VPI, it accelerates the discovery of infiltration profiles that are robust to coupled reaction–diffusion dynamics. The approach is computationally efficient, relying on vectorized moment calculations and adaptive exploration strategies that avoid costly Monte Carlo approximations. At the same time, the framework is flexible and can be applied to a broad range of functional optimization problems beyond the case studies considered here.

The work also has limitations. The assumption of independence among functional principal component scores, while justified empirically in our data, may not hold in all settings. Extending the method to correlated scores through multi-output Gaussian processes remains an important direction, albeit at higher computational costs. Similarly, the scalability of the approach with respect to the number of retained components M warrants further study, since error statistics grow quadratically with M . Finally, while our acquisition adapts dynamically, additional research is needed to better understand exploration–exploitation trade-offs in high-dimensional functional spaces.

In summary, this work advances BO by directly addressing functional responses under worst-case criteria. Our method unites functional representation, probabilistic modeling, and robust acquisition into a tractable framework that is both theoretically grounded and practically effective. We anticipate that these ideas will stimulate further research at the interface of functional data analysis, robust optimization, and machine learning for scientific discovery.

References

- Antonio Candelieri. A gentle introduction to bayesian optimization. In *Winter Simulation Conference*, 2021.
- Eleonora Cara, Irdi Murataj, Gianluca Milano, Natascia De Leo, Luca Boarino, and Federico Ferrarese Lupi. Recent advances in sequential infiltration synthesis applications using block copolymers. *Nanomaterials*, 11(4):994, 2021.
- Mingkun Chen, Robert Lupoiu, Chenkai Mao, Der-Han Huang, Jiaqi Jiang, Philippe Lalanne, and Jonathan A Fan. High speed simulation and freeform optimization of nanophotonic devices with physics-augmented deep learning. *ACS Photonics*, 9(9):3110–3123, 2022.
- Weiting T Chen, Alexander Q Zhu, and Federico Capasso. Flat optics with dispersion engineered metasurfaces. *Nature Reviews Materials*, 5:604–620, 2020.
- Taewon Choi, Chulsoo Choi, Junseo Bang, Youngjin Kim, Hyunwoo Son, Changhyun Kim, Junhyeok Jang, Yoonchan Jeong, and ByoungHo Lee. Multiwavelength achromatic deflector in the visible using a single-layer freeform metasurface. *Nano Letters*, 24(35):10980–10986, 2024.

- Stefano Conti and Anthony O’Hagan. Bayesian emulation of complex multi-output and dynamic computer models. *Journal of Statistical Planning and Inference*, 140(3):640–651, 2010.
- Chaofan Huang, Yi Ren, Emily K McGuinness, Mark D Losego, Ryan P Lively, and V Roshan Joseph. Bayesian optimization of functional output in inverse problems. *Optimization and Engineering*, 22(4):2553–2574, 2021.
- Donald R Jones, Matthias Schonlau, and William J Welch. Efficient global optimization of expensive black-box functions. *Journal of Global Optimization*, 13(4):455–492, 1998.
- Harit Keawmuang, Shiqi Hu, Trevon Badloe, Sunae So, and Junsuk Rho. Hybrid frameworks integrating deep learning and optimization methods for inverse design in nanophotonics. *ACS Applied Materials & Interfaces*, 2025.
- Yashar Kiarashinejad, Sajjad Abdollahramezani, and Ali Adibi. Deep learning approach based on dimensionality reduction for designing electromagnetic nanostructures. *npj Computational Materials*, 6(1):12, 2020.
- Alexander V Kildishev, Alexandra Boltasseva, and Vladimir M Shalaev. Planar photonics with metasurfaces. *Science*, 339(6125):1232009, 2013.
- Lars Kotthoff, Hud Wahab, and Patrick A Johnson. Bayesian optimization in materials science: A survey. *arXiv preprint*, 2021.
- Zhaxylyk A Kudyshev, Alexander V Kildishev, Vladimir M Shalaev, and Alexandra Boltasseva. Machine learning-assisted global optimization of photonic devices. *Nanophotonics*, 10(1):371–383, 2020.
- Collen Z Leng and Mark D Losego. Vapor phase infiltration for transforming polymers into organic inorganic hybrid materials. *Materials Horizons*, 4(5):747–771, 2017.
- Qiaohao Liang, Aldair E Gongora, Zekun Ren, Armi Tiihonen, Zhe Liu, Shijing Sun, James R Deneault, Daniil Bash, Flore Mekki-Berrada, Saif A Khan, Kedar Hippalgaonkar, Benji Maruyama, Keith A Brown, John Fisher III, and Tonio Buonassisi. Benchmarking the performance of bayesian optimization across multiple experimental materials science domains. *npj Computational Materials*, 7, 2021.
- Reza Marzban, Hamed Abiri, Raphaël Pestourie, and Ali Adibi. Hilab: A hybrid inverse-design framework. *Small Methods*, page e00975, 2025a.
- Reza Marzban, Ali Adibi, and Raphael Pestourie. Inverse design in nanophotonics via representation learning. *arXiv preprint arXiv:2507.00546*, 2025b.
- Reza Marzban, Ashkan Zandi, and Ali Adibi. Gibbs: Generative input-side basis-driven structures. *arXiv preprint arXiv:2511.07339*, 2025c.
- Sean Molesky, Zin Lin, Alexander Y Piggott, Weiliang Jin, Jelena Vucković, and Alejandro W Rodriguez. Inverse design in nanophotonics. *Nature Photonics*, 12(11):659–670, 2018.

- Jeffrey S Morris. Functional regression. *Annual Review of Statistics and Its Application*, 2(1):321–359, 2015.
- Joel A Paulson, Georgios Makrygiorgos, and Ali Mesbah. Adversarially robust bayesian optimization for efficient auto tuning of generic control structures under uncertainty. *AIChE Journal*, 68(6):e17591, 2022.
- Raphaël Pestourie, Carlos Pérez-Arancibia, Zin Lin, Wonseok Shin, Federico Capasso, and Steven G Johnson. Inverse design of large-area metasurfaces. *Optics express*, 26(26):33732–33747, 2018.
- Thomas W Radford, Peter R Wiecha, Alberto Politi, Ioannis Zeimpekis, and Otto L Muskens. Inverse design of unitary transmission matrices in silicon photonic coupled waveguide arrays using a neural adjoint model. *ACS photonics*, 12(3):1480–1493, 2025.
- Yi Ren, Emily K McGuinness, Chaofan Huang, V Roshan Joseph, Ryan P Lively, and Mark D Losego. Reaction diffusion transport model to predict precursor uptake and spatial distribution in vapor phase infiltration processes. *Chemistry of Materials*, 33(13):5210–5222, 2021.
- Bobak Shahriari, Kevin Swersky, Ziyu Wang, Ryan P Adams, and Nando de Freitas. Taking the human out of the loop: A review of bayesian optimization. *Proceedings of the IEEE*, 104(1):148–175, 2016.
- Ruben Z Waldman, David J Mandia, Angel Yanguas–Gil, Alex B F Martinson, Jeffrey W Elam, and Seth B Darling. The chemical physics of sequential infiltration synthesis: A thermodynamic and kinetic perspective. *Journal of Chemical Physics*, 151(19):190901, 2019.
- Xilu Wang, Yaochu Jin, Sebastian Schmitt, and Markus Olhofer. Recent advances in bayesian optimization. *ACM Computing Surveys*, 55(13s):1–36, 2023.
- Dorina Weichert and Alexander Kister. Bayesian optimization for min max optimization. *arXiv preprint*, 2021.
- Dorina Weichert, Alexander Kister, Patrick Link, Sebastian Houben, and Gunar Ernis. Robust entropy search for safe efficient bayesian optimization. In *Conference on Uncertainty in Artificial Intelligence*, volume 244 of *Proceedings of Machine Learning Research*, page 3711–3729, 2024.
- Lin Yang, Junlong Lyu, Wenlong Lyu, and Zhitang Chen. Efficient robust bayesian optimization for arbitrary uncertain inputs. In *Advances in Neural Information Processing Systems*, 2023.
- Nanfang Yu and Federico Capasso. Flat optics with designer metasurfaces. *Nature Materials*, 13:139–150, 2014.
- Mohammadreza Zandehshahvar, Yashar Kiarashinejad, Muliang Zhu, Hossein Maleki, Tyler Brown, and Ali Adibi. Manifold learning for knowledge discovery and intelligent inverse

design of photonic nanostructures: breaking the geometric complexity. *Acs Photonics*, 9 (2):714–721, 2022.

Appendix A.

In this appendix, we prove Proposition 1:

Proof Fix $\theta \in \Theta$. For any $\lambda \in \Lambda$ choose an index $m(\lambda) \in \{1, \dots, T\}$ with $|\lambda - \lambda_{m(\lambda)}| \leq h_T$. By the modulus of continuity,

$$e(\theta, \lambda) \leq e(\theta, \lambda_{m(\lambda)}) + \omega(|\lambda - \lambda_{m(\lambda)}|) \leq \max_{1 \leq m \leq T} e(\theta, \lambda_m) + \omega(h_T).$$

Taking the supremum over λ gives

$$g(\theta) = \sup_{\lambda \in \Lambda} e(\theta, \lambda) \leq \max_{1 \leq m \leq T} e(\theta, \lambda_m) + \omega(h_T) = g_T(\theta) + \omega(h_T),$$

hence $0 \leq g(\theta) - g_T(\theta) \leq \omega(h_T)$. When $e(\theta, \lambda)$ is Lipschitz in λ uniformly in θ with constant L , the modulus can be chosen as $\omega(r) = Lr$, which gives the Lipschitz bound. For a one-dimensional equally spaced grid on $[a, b]$ with spacing $\Delta = (b - a)/(T - 1)$, the maximal gap from any λ to its nearest grid point is $\Delta/2$, so $h_T = \Delta/2$. Substituting yields

$$g(\theta) - g_T(\theta) \leq \omega(\Delta/2), \quad \text{and, if Lipschitz, } g(\theta) - g_T(\theta) \leq \frac{L}{2} \Delta. \quad \blacksquare$$

Appendix B.

In this appendix, we prove Theorem 2:

Proof Fix $\theta \in \Theta$ and write

$$\Delta_t(\theta) = \sup_{\lambda \in \Lambda} |\mu_{e,t}(\theta, \lambda) - e(\theta, \lambda)|, \quad U_t(\theta) = \int_{\Lambda} \sigma_{e,t}(\theta, \lambda) d\nu(\lambda).$$

Step 1: pointwise bound. Since $-\kappa_t U_t(\theta) \leq 0$,

$$\alpha_t(\theta) - g(\theta) = \sup_{\lambda} \mu_{e,t}(\theta, \lambda) - \kappa_t U_t(\theta) - \sup_{\lambda} e(\theta, \lambda) \leq \sup_{\lambda} (\mu_{e,t}(\theta, \lambda) - e(\theta, \lambda)) \leq \Delta_t(\theta).$$

Also,

$$g(\theta) - \alpha_t(\theta) = \sup_{\lambda} e(\theta, \lambda) - \sup_{\lambda} \mu_{e,t}(\theta, \lambda) + \kappa_t U_t(\theta) \leq \sup_{\lambda} (e(\theta, \lambda) - \mu_{e,t}(\theta, \lambda)) + \kappa_t U_t(\theta) \leq \Delta_t(\theta) + \kappa_t U_t(\theta).$$

Combining the two displays gives

$$|\alpha_t(\theta) - g(\theta)| \leq \Delta_t(\theta) + \kappa_t U_t(\theta).$$

Step 2: uniform convergence. Taking $\sup_{\theta \in \Theta}$ and using assumptions (i) to (iii),

$$\sup_{\theta \in \Theta} |\alpha_t(\theta) - g(\theta)| \leq \sup_{\theta} \Delta_t(\theta) + \left(\sup_t \kappa_t \right) \sup_{\theta} U_t(\theta) \rightarrow 0.$$

Step 3: convergence of near minimizers. Let θ_t satisfy $\alpha_t(\theta_t) \leq \inf_{\theta} \alpha_t(\theta) + \varepsilon_t$ with $\varepsilon_t \rightarrow 0$, and let $\bar{\theta}$ be any limit point of $\{\theta_t\}$. Uniform convergence implies

$$\limsup_{t \rightarrow \infty} g(\theta_t) \leq \limsup_{t \rightarrow \infty} (\alpha_t(\theta_t) + \|\alpha_t - g\|_{\infty}) \leq \limsup_{t \rightarrow \infty} \inf_{\theta} \alpha_t(\theta) = \inf_{\theta} g(\theta),$$

where the last equality uses uniform convergence again. By continuity of g and compactness of Θ , $g(\bar{\theta}) \leq \inf_{\theta} g(\theta)$, hence $\bar{\theta}$ minimizes g . \blacksquare